HHS Public Access

Author manuscript

Magn Reson Med. Author manuscript; available in PMC 2018 January 01.

Published in final edited form as:

Magn Reson Med. 2017 January ; 77(1): 229–236. doi:10.1002/mrm.26114.

Measuring B_1 distributions by B_1 phase encoding

Kalina V. Jordanova, **Dwight G. Nishimura**, and **Adam B. Kerr**

Magnetic Resonance Systems Research Laboratory, Department of Electrical Engineering, Stanford University, Stanford, California

Abstract

Purpose—We propose a method to acquire B_1 distribution plots by encoding in B_1 instead of image space. Using this method, B_1 data is acquired in a different way from traditional spatial B_1 mapping, and allows for quick measurement of high dynamic range B_1 data.

Methods—To encode in B_1, we acquire multiple projections of a slice, each along the same direction, but using a different phase sensitivity to B_1. Using a convex optimization formulation, we reconstruct histograms of the B_1 distribution estimates of the slice.

Results—We verify in vivo B_1 distribution measurements by comparing measured distributions to distributions calculated from reference spatial B_1 maps using the Earth Mover's Distance (EMD). Phantom measurements using a surface coil show that for increased spatial B_1 variations, measured B_1 distributions using the proposed method more accurately estimate the distribution than a low-resolution spatial B_1 map, resulting in a 37% EMD decrease while using fewer measurements.

Conclusion—We propose and validate the performance of a method to acquire B_1 distribution information directly without acquiring a spatial B_1 map. The method may provide faster estimates of a B_1 field for applications that do not require spatial B_1 localization, such as the transmit gain calibration of the scanner, particularly for high dynamic B_1 ranges.

Keywords

B_1 distributions; B_1 mapping

Introduction

In magnetic resonance imaging (MRI), mapping the transmit radiofrequency (B_1) field is important for a variety of applications, including calibrating the transmit gain of the scanner, measuring coil performance, and parallel transmit pulse design [1, 2]. To visualize B_1 field variations in a volume, a spatial B_1 map is often acquired and displayed as two-dimensional (2D) images. There exist a variety of methods for spatial B_1 mapping, categorized as either signal magnitude-based [3–10] or signal phase-based [11–16] methods.

Address correspondence to: Kalina Jordanova, MS, Packard Electrical Engineering, Room 208, 350 Serra Mall, Stanford, CA 94305-9510, kalinaj@stanford.edu.

We propose a method to acquire B_1 distribution plots that estimate the histogram of B_1 values in a volume, rather than acquiring spatial B_1 maps. B_1 distribution plots may offer benefits over traditional spatial B_1 mapping methods when spatial localization of the B_1 field is not necessary, and knowledge of the distribution of B_1 in the volume suffices (e.g., for the scanner transmit gain calibration). Distribution measurements may be useful for nonproton imaging, where rapid measurement of the B_1 field is important [17–19], or for volumes with very rapid spatial B_1 variations that may experience unwanted intra-voxel signal averaging with spatial mapping techniques.

We propose a B_1 distribution measurement method that uses an existing signal phase-based B_1 mapping method, BEAR [15]. When acquiring a spatial B_1 map, BEAR is insensitive to T_1, T_2, repetition time (TR) and off-resonance frequency variations, and allows for direct mapping between signal phase and B_1. Another important property of BEAR is the easily tunable, approximately linear, phase sensitivity to B_1 variations. The proposed method acquires a series of BEAR projection measurements using different phase sensitivities to B_1, so that the result is an acquisition which has phase-encoding as a function of B_1, rather than as a function of image space. We describe the theory behind the acquisition and reconstruction of the proposed technique, and validate the method in vivo at 3T and with a phantom at 1.5T.

Theory

Phase sensitivity tuning

This study uses the BEAR method [15, 20], a phase-based B_1 mapping method, to encode B_1 variations into an MR signal. Figure 1a shows the BEAR sequence diagram with two adiabatic full passage HSn pulses [21] that have different relative peak magnitudes, and different magnitude and frequency sweep shapes, which are determined by the parameters n_1 and n_2. These two HSn pulses create a twice-refocused spin-echo whose phase is proportional to B_1. The particular choice of n_2 given n_1 is determined by minimizing any residual phase error over the HSn pulse bandwidth and a B_1 range of choice [20].

Figure 1b shows the phase sensitivity to B_1, which can be varied by varying the magnitude ratio between the HSn pulses, δ. In this study, we denote changes in phase sensitivity by specifying the parameter δ, however, in practice n_2 also slightly varies because the sequence is re-optimized for each δ to better minimize any residual phase error [20]. The phase relationship to B_1 is approximately linear above the adiabatic threshold of the sequence. We refer to the slope of a first-degree polynomial fit of the phase relationship to B_1 simply as the sensitivity, α. Table 1 summarizes δ, n_2, and α for this study.

B_1 distribution plots

Figure 2a shows a comparison of a typical 2D B_1 map to an example B_1 distribution plot. A distribution plot essentially shows the distribution of B_1 values seen in a volume or slice, as shown in Figure 2a. When compared to a spatial B_1 map of the same imaging region, distribution plots consist of histograms of the B_1 values seen along one axis/several axes of choice. For example, in Figure 2a, the B_1 values seen over each horizontal line in the 2D B_1

map are represented by a B_1 histogram in the B_1 distribution plot, and are displayed as a horizontal line at the same original vertical location as in the 2D map. Thus, in Figure 2a, the B_1 distributions represent the B_1 values seen along the x-axis of the 2D map.

Figure 2b illustrates the theory for acquiring an MR signal with phase-encoding as a function of B_1 rather than spatial position. Given unknown B_1 values in a slice (represented by the 2D map of Figure 2b.i), we acquire multiple projection measurements, each along the same direction but using a different phase sensitivity. In the example illustrated in Figure 2b, the projection direction is always along the x-axis, whereas y is in the readout direction of the sequence. Two projections are acquired for each phase sensitivity, the second with the order of the HSn pulses reversed, so that unwanted phase sources can be removed by taking the phase difference between the two acquisitions. Figure 2b.ii shows example phases of acquired k-space MR signals for $\delta = [0.8, 0.94, 1]$. 1D inverse Fourier transforms along k_y, and phase differences are calculated for each δ, which result in the final acquired projections that exhibit B_1 phase-encoding (Figure 2b.iii). These are used to calculate the B_1 distribution plot (Figure 2b.iv). The B_1 distribution plots displayed in this study are normalized so that each histogram sums to one for each y location.

An estimate of the B_1 distribution is calculated using the acquired projections and the known phase sensitivity to B_1 for each projection. A B_1 distribution for the slice seen at one y position can be binned into a histogram with K bins, with each bin representing a particular B_1 range, $B_{1,k}$. The fraction of spins in the slice with $B_1 \in B_{1,k}$ is c_k. Given J total projection measurements, each with a known phase sensitivity to B_1, $\phi_j(B_1)$, then the j^{th} acquired projection is:

$$p_j = \sum_{k=1}^{K} c_k e^{i\phi_{j,k}} \quad (1)$$

where $\phi_{j,k} = \phi_j(B_{1,k})$. This can be simplified into matrix form as:

$$\begin{bmatrix} p_1 \\ p_2 \\ \vdots \\ p_J \end{bmatrix} = \begin{bmatrix} e^{i\phi_{1,1}} & e^{i\phi_{1,2}} & \cdots & e^{i\phi_{1,K}} \\ e^{i\phi_{2,1}} & e^{i\phi_{2,2}} & \cdots & e^{i\phi_{2,K}} \\ \vdots & \vdots & \ddots & \vdots \\ e^{i\phi_{J,1}} & e^{i\phi_{J,2}} & \cdots & e^{i\phi_{J,K}} \end{bmatrix} \begin{bmatrix} c_1 \\ c_2 \\ \vdots \\ c_K \end{bmatrix} \quad (2)$$

or equivalently:

$$\mathbf{p} = \mathbf{\Phi c} \quad (3)$$

where **p** and **c** are vectors that contain the measured projections and unknown B_1 distribution fractions, respectively, and **Φ** is a phase matrix calculated from the known phase sensitivities and chosen B_1 histogram bin centers.

While the phase-based BEAR method is independent of T_1 and T_2, the actual B_1 distribution frequencies are based on signal magnitude, and will therefore be affected by T_1, T_2 and the excitation B_1. Note that the maxima and minima B_1 values can still be measured independently of these factors. The B_1 dependence on the magnetization can be approximated in Equation 2 by adding a magnitude term into $\mathbf{\Phi}$ that represents the effective tip angle at the B_1 bin centers, however, in practice we have found this addition to provide no appreciable improvement on the results of this study. It may be possible to model T_1 and T_2 effects if there is prior knowledge of these parameters for the imaging region. For this study, we assume a homogenous sample that does not have magnitude weighting from T_1 and T_2, and use the basic representation shown in Equation 3.

The form of $\mathbf{\Phi}$ in Equation 2 is similar to a typical discrete Fourier transform matrix, often used for spatial imaging in MRI. However, here $\mathbf{c}$ relates to the ratio of spins with respect to B_1 bins, rather than to spatial position.

With the measured projections, $\mathbf{p}$, and known phase sensitivities, $\mathbf{\Phi}$, Equation 3 has only one unknown: the B_1 distribution vector $\mathbf{c}$. A simple inversion of $\mathbf{\Phi}$ can be used to solve for $\mathbf{c}$: $\mathbf{c}=\mathbf{\Phi}^{-1}\mathbf{p}$, however, in practice the performance of this method is improved by introducing constraints in the form of a convex optimization problem. $\mathbf{c}$ can be found by minimizing the difference between $\mathbf{p}$ and $\mathbf{\Phi c}$: $\min_{\mathbf{c}} f(\mathbf{p}-\mathbf{\Phi c})$, where $f()$ is a chosen cost function. To improve the performance of the optimization, we create a scalarized multi-objective problem by introducing smoothing via finite second derivative matrices $\lambda_1\mathbf{D}_1$ and $\lambda_2\mathbf{D}_2$, which smooth along the B_1 and readout dimensions respectively, as is expected of typical B_1 distributions. For a more robust performance against noise, we also add constraints limiting the size of $\mathbf{c}$ and ensuring that $\mathbf{c}$ is nonnegative real. The final problem is formulated as:

$$\begin{aligned}&\underset{\mathbf{c}}{\text{minimize}} \sum \mathrm{h}(\mathbf{p}-\mathbf{\Phi c})+\lambda_1\sum \mathrm{h}(\mathbf{D}_1\mathbf{c})+\lambda_2\sum \mathrm{h}(\mathbf{D}_2\mathbf{c})+\lambda_3\mathbf{1}^T\mathbf{c}\\ &\text{subject to } \mathbf{c}\geq 0\end{aligned} \tag{4}$$

where h() is the Huber loss function with $\mathrm{h}(x)=x^2$ for $x\leq 1$ and $\mathrm{h}(x)=2|x|-1$ for $x\geq 1$, and is used to reduce sensitivity to outliers, and $\mathbf{1}$ is a vector of ones.

Methods

Parameter selection

The HSn parameters were chosen as in reference [20], with 773 Hz pulse bandwidth. For imaging, K = 11 B_1 bins and J = 11 sensitivities, uniformly distributed in the range of δ = [0.8, 1], were used. The δ range of the HSn pulses was chosen to maximize the range of phase sensitivities, while remaining insensitive to the adiabatic threshold of the sequence, ~$0.051/\delta$ G. The expected B_1 range over which n_2 was optimized was (1±0.2)0.086 G for 1.5T and (1±0.4)0.12 G for 3T. The chosen δs and resulting n_2s and αs are shown in Table 1.

The range of sensitivities used is analogous to the amount of k_y excursion in traditional Fourier imaging, while the number of B_1 bins is analogous to the number of phase encodes.

Following this analogy and examining Equation 2, the field of view in B_1 is approximately $2\pi/\Delta\alpha_{max}$, where $\Delta\alpha_{max}$ is the maximum sensitivity difference between successive δ values, and the resolution in B_1 is approximately $2\pi/(\alpha_{max}-\alpha_{min})$, where α_{max} and α_{min} are the maximum and minimum phase sensitivities. For the parameters chosen here, this results in a B_1 resolution of 0.069/0.064 G and field of view of 0.68/0.63 G for 1.5/3T respectively. Increasing the number of B_1 bins may improve the resolution of the measurements, at the cost of increased scan time. In practice, using the optimization formulation of Equation 4, we can improve on the expected B_1 resolution. We use a B_1 range of 0.136 G and 11 bins, giving a B_1 resolution of 0.012 G, which we have found to produce good results despite pushing the method beyond the theoretical expectations with the Fourier imaging comparison.

Projection acquisition

In vivo scans used a 3T General Electric (GE) Discovery MR750 scanner with a transmit body coil and receive head coil. B_1 distribution plots were acquired with 11 B_1 bins and a readout size of 128. Additionally, 128×128 2D B_1 maps were acquired for reference with a field of view of 24 cm. All scans used a single-slice acquisition protocol with a 40° excitation tip angle, 44 ms echo time, and TR = 500 ms. The distribution scans acquired 22 measurements, two for each δ, giving a total theoretical scan time of 11 s, while the 2D maps had a total scan time of about 2 min. The implementation of the method was such that δ was manually changed for each scan, resulting in a slight pause between successive scans and an effective scan time longer than 11 s for the distribution plots. For all scans, the adiabatic pulses were non-selective and a single signal acquisition was used.

Phantom scans used a 1.5T GE Signa Excite scanner with a transmit/receive surface coil. Imaging used a slice oblique to the orientation of the surface coil to test the performance of the method for a B_1 field that has increased spatial variations. A wire was placed along the surface of the phantom to simulate increased B_1 variations in the presence of a guidewire. The B_1 distribution plots used 11 B_1 bins and a readout size of 64. 2D B_1 maps were acquired at two different matrix sizes: 64×64 and 16×16, with a field of view of 8 cm. TR = 200 ms and the total theoretical scan time was 4.4 seconds for the distribution plots, and less than a minute for the 2D maps. All remaining scanning parameters were the same as for the in vivo scans at 3T.

B_1 distribution reconstruction

The projection for $\delta = 1$ did not have B_1 encoding and was used to create a mask in y by excluding pixels with signal less than 3% of the maximum. $\mathbf{\Phi}$ was calculated using B_1 bin centers uniformly spaced between [0.017, 0.153] G, with $\phi_{j,k}=\phi_j(B_{1,k})$. Although the phase relationship to B_1 can be approximated by α, in practice, we used Bloch simulations to determine $\phi_j(B_{1,k})$. For the optimization, each regularization parameter λ was successively selected by searching over a parameter space, and the optimal value was chosen located near the L-curve corner when plotting the λ regularization against the Huber penalty result. The proposed method was solved using the CVX package [22, 23].

To evaluate the accuracy of the measured B_1 distributions, we created B_1 histograms from the 2D B_1 maps over the same projection direction. To compare distributions calculated from 2D maps and those created using the proposed method, the Earth Mover's Distance (EMD) [24] metric was calculated for each y location, which estimates the work needed to transform one distribution into the other. A smaller EMD value indicates greater similarity between distributions.

Results

For each set of data in Figures 3 and 4, the columns show, from left to right: acquired 2D B_1 maps for reference, B_1 distribution plots calculated from the 2D maps, B_1 distribution plots using the method proposed here, and the EMD calculated between the two distributions for each y location.

In vivo results at 3T are shown in Figure 3. The B_1 distributions using the proposed method closely match the distributions from the 2D maps, and exhibit low average EMD values of [0.0022, 0.0034] G*(Relative frequency) over a 0.136 G B_1 range and with 0.012 G B_1 bins.

The phantom results obtained at 1.5T were examined to assess the performance of the proposed method when there are increased spatial B_1 variations and are shown in Figure 4a. A B_1 distribution is calculated from the 64×64 resolution 2D B_1 map. The B_1 distribution using the 16×16 2D B_1 map varies from the 64×64 resolution distribution, due to intra-voxel averaging of the phase. Additionally, because of the high B_1 range, phase unwrapping must be employed, as can be seen in Figure 4b. For the low-resolution image, without prior knowledge of the B_1 range, phase unwrapping is not easily achieved due to increased intra-voxel averaging. This results in increased inaccuracies in the resulting low-resolution B_1 map. To compare the high- and low-resolution distributions, the EMD is calculated by piecewise constant interpolation of the low-resolution image, and is 0.0202 G*(Relative frequency). Alternatively, the B_1 distribution plot that uses the proposed method more closely matches the B_1 distribution of the 64×64 2D map with EMD = 0.0136 G*(Relative frequency), even though it uses fewer measurements than the 16×16 2D map (11 measurements for the measured distribution, 16 measurements for the 2D map). This indicates that the proposed method provides a good approximation of the B_1 distribution for the slice using a small number of measurements.

Discussion

We have demonstrated a new method that estimates the B_1 distribution in a slice without acquiring 2D image data. By encoding the MR signal as a function of B_1, we were able to acquire B_1 distribution measurements that correlated well with distributions calculated from 2D B_1 maps. Most of the errors are concentrated along the B_1 distribution, suggesting the errors are most likely due to misplaced counts in consecutive bins, with only small errors in the underlying B_1.

The convex optimization formulation was shown to be accurate for both the in vivo and phantom measurements in this study, but additional constraints may improve the

performance of the method. The optimization formulation is a general approach, allowing for more B_1 bins than number of encodings, and also for nonuniform binning.

The B_1 distribution measurements represent relative B_1 frequency based on signal magnitude, rather than volume. While the phase-based BEAR method is independent of T_1 and T_2, the actual distribution frequencies will be affected by the signal magnitude, and therefore by anything that affects the signal magnitude, e.g., T_1, T_2, the excitation B_1, proton density and the receive coil sensitivity. Nevertheless, the method can measure the extrema of the B_1 distribution. Furthermore, the signal magnitude dependence on flip angle, due to variations in the excitation B_1, can be approximated in Equation 2 by adding a magnitude term into $\mathbf{\Phi}$ that represents the effective tip angle at the B_1 bin centers. It may be possible to minimize T_1 and T_2 effects on the signal magnitude by imaging with a longer TR and minimized TE, respectively; however, the effects of proton density and receive coil sensitivity on the signal magnitude cannot be removed. We have demonstrated in this study that the B_1 distribution itself can be accurately measured even using the basic optimization formulation presented here.

The proposed method will in general require fewer measurements than acquiring a full spatial B_1 map. For example, the B_1 distributions measured in this study required 11 B_1 encoding measurements, versus 128 phase encodes for the 2D map. Note, however, that the time needed for spatial B_1 mapping may be decreased by using efficient acquisition strategies, such as echo-planar imaging. This is not the case for the proposed method, because the nature of the B_1 encoding requires an individual excitation for each acquired projection with a different phase sensitivity.

With 11 B_1 encodings we found the method measured B_1 distributions accurately for in vivo measurements at 3T compared to distributions calculated from 2D B_1 maps. We interpolated δ linearly in the range of [0.8, 1], however any number of encodings, δ range, and nonlinear interpolation can be used. Ideally, the δ range would be chosen to approximate the same phase encoding in Equation 2 as a typical discrete Fourier transform. For example, the phase of a discrete Fourier transform is $2\pi nk/N$, where n and k vary from [0, N-1] and represent the indices over the signal's spatial and frequency components. The maximum phase is therefore $2\pi(N-1)^2/N$, corresponding to 57.1 rad for $N = 11$. Using the HSn pulses described here, there is a maximum phase change of 12.3 rad for ±20% variation in B_1 at 1.5T, and 13.4 rad for ±40% variation in B_1 at 3T. Even though this is less than the theoretical amount of phase variation that would be needed for the discrete Fourier transform to reach the same resolution, by including regularization in the optimization problem we have found the method to perform well. Future implementations could increase the phase sensitivity by increasing n or decreasing δ.

The proposed method was able to measure increased spatial B_1 variations in a phantom at 1.5T with the presence of a wire. The B_1 distributions using the proposed method had better approximations of the B_1 distribution from 2D maps when compared to a low-resolution spatial map of the same slice. This is due to intra-voxel phase averaging for the low-resolution image. This results in increased B_1 errors because a larger voxel encompasses a larger B_1 range and will therefore have more dephasing, and also because phase unwrapping

was difficult to employ for the low-resolution phase image. Phase wrapping occurs due to the very large B_1 range seen in the slice, even though a relatively low sensitivity ($\delta = 0.9$) was used to acquire the images. To reduce phase wrapping, a lower sensitivity may be used, but would come at the cost of decreased B_1-to-noise ratio.

For very low B_1 values below the sequence adiabatic threshold, the phase dependence on B_1 will be nonlinear and the measurements will be expected to have increased noise due to low phase sensitivity. It is possible to decrease the adiabatic threshold by using higher n or δ, at the cost of potentially increased errors within the bandwidth of the pulses, or lower phase sensitivity to B_1. An analysis of the effect of decreased B_1 values below the adiabatic threshold conducted in the original BEAR paper [15] illustrated that the largest effect on the acquired signal comes from the decrease in the magnitude of the signal below the adiabatic threshold. For the HSn pulses used in this study, a decrease of 50% in the expected refocused magnitude occurs for $B_1 \sim 56\%$ of the adiabatic threshold. Finally, we assume that the MR system will be able to generate signal at B_1 values in the ranges above the adiabatic thresholds described here. If a system is unable to generate such peak RF values, this method will suffer. Note however, that when assuming linearity of the RF system, as is typically done for B_1 mapping, measuring B_1 in a range that is higher than will be used for subsequent scans is still useful for calibration of the transmit system.

The BEAR method's reliable formation of a twice-refocused spin-echo signal makes it especially useful for this application, since it will not experience unwanted phase cancellation over the projected volume due to off-resonance effects, and it allows for robust refocusing independent of B_1 variations. Other phase-based B_1 mapping methods that allow for a spin-echo acquisition could also be used in a similar manner to acquire B_1 distribution measurements. Magnitude-based methods may also be used, although care must be taken to mitigate relaxation effects.

Compared to 2D B_1 mapping methods, the proposed B_1 distribution method may be useful to acquire faster estimates of the B_1 distribution in a volume, or to estimate a distribution where B_1 is varying rapidly spatially, such as near a conducting guidewire. In this study we acquired B_1 distributions over a slice, however, it is possible to apply this method over a 3D volume to get B_1 distributions for the entire volume, which may be useful for the transmit gain calibration of the scanner. This method may be particularly useful for acquiring a quick preliminary scan to determine the RF scaling and B_1 range required for any subsequent spatial mapping methods; for example, in setting the RF amplitude of any subsequent adiabatic pulses.

Conclusion

We demonstrated a new method for acquiring B_1 distributions in a slice without acquiring full spatial image data, by encoding the signal in B_1. We validated the performance of the method in vivo, and in a phantom study with increased spatial variations in B_1. The optimization formulation used in this study was a basic formulation that was shown to produce accurate distribution estimates, however, improvements in the problem formulation, especially with respect to T_1, T_2, and B_1 dependence, may lead to improved performance.

This method could be useful for acquiring fast estimates of the B_1 distribution in a volume, particularly where there is a high dynamic B_1 range within the imaging region. This distribution information could also be useful for the transmit gain calibration of the scanner.

Acknowledgments

The authors thank Bob Dougherty for access to the Stanford Center for Cognitive and Neurobiological Imaging's 3T scanner.

Grant sponsor: National Science Foundation; Grant number: DGE-1147470; Grant sponsor: National Institutes of Health; Grant number: R01EB008108.

References

1. Katscher U, Börnert P, Leussler C, van den Brink JS. Transmit SENSE. Magn Reson Med. 2003; 49:144–150. [PubMed: 12509830]
2. Zhu Y. Parallel excitation with an array of transmit coils. Magn Reson Med. 2004; 51:775–784. [PubMed: 15065251]
3. Hornak JP, Szumowski J, Bryant RG. Magnetic field mapping. Magn Reson Med. 1988; 6:158–163. [PubMed: 3367773]
4. Akoka S, Franconi F, Seguin F, LePape A. Radiofrequency map of an NMR coil by imaging. Magnetic Resonance Imaging. 1993; 11:437–441. [PubMed: 8505878]
5. Insko EK, Bolinger L. Mapping of the radiofrequency field. Journal of Magnetic Resonance, Series A. 1993; 103:82–85.
6. Stollberger R, Wach P. Imaging of the active B1 field in vivo. Magn Reson Med. 1996; 35:246–251. [PubMed: 8622590]
7. Cunningham CH, Pauly JM, Nayak KS. Saturated double-angle method for rapid B1+ mapping. Magn Reson Med. 2006; 55:1326–1333. [PubMed: 16683260]
8. Dowell NG, Tofts PS. Fast, accurate, and precise mapping of the RF field in vivo using the 180° signal null. Magn Reson Med. 2007; 58:622–630. [PubMed: 17763355]
9. Yarnykh VL. Actual flip-angle imaging in the pulsed steady state: A method for rapid three-dimensional mapping of the transmitted radiofrequency field. Magn Reson Med. 2007; 57:192–200. [PubMed: 17191242]
10. Nehrke K, Börnert P. DREAM-a novel approach for robust, ultrafast, multislice B1 mapping. Magn Reson Med. 2012; 68:1517–1526. [PubMed: 22252850]
11. Morrell GR. A phase-sensitive method of flip angle mapping. Magn Reson Med. 2008; 60:889–894. [PubMed: 18816809]
12. Hennel F, Köhler S. Improved phase-based adiabatic B1 mapping. Proc Int Soc Magn Reson Med. 2010; 18:237.
13. Sacolick LI, Wiesinger F, Hancu I, Vogel MW. B1 mapping by Bloch-Siegert shift. Magn Reson Med. 2010; 63:1315–1322. [PubMed: 20432302]
14. Chang YV. Rapid B1 mapping using orthogonal, equal-amplitude radio-frequency pulses. Magn Reson Med. 2012; 67:718–723. [PubMed: 21713982]
15. Jordanova KV, Nishimura DG, Kerr AB. B1 estimation using adiabatic refocusing: BEAR. Magn Reson Med. 2014; 72:1302–1310. [PubMed: 24272817]
16. Lee Y, Han Y, Park H, Watanabe H, Garwood M, Park JY. New phase-based B1 mapping method using two-dimensional spin-echo imaging with hyperbolic secant pulses. Magn Reson Med. 2015; 73:170–181. [PubMed: 24459088]
17. Hancu I, Watkins R, Kohler SJ, Mallozzi RP. Accurate flip-angle calibration for 13C MRI. Magn Reson Med. 2007; 58:128–133. [PubMed: 17659619]
18. Bashir A, Conradi MS, Woods JC, Quirk JD, Yablonskiy DA. Calibration of RF transmitter voltages for hyperpolarized gas MRI. Magn Reson Med. 2009; 61:239–243. [PubMed: 19097199]

19. Schulte RF, Sacolick L, Deppe MH, Janich MA, Schwaiger M, Wild JM, Wiesinger F. Transmit gain calibration for nonproton MR using the Bloch-Siegert shift. NMR in Biomedicine. 2011; 24:1068–1072. [PubMed: 21387441]
20. Jordanova KV, Nishimura DG, Kerr AB. Lowering the B1 threshold for improved BEAR B1 mapping. Magn Reson Med. 2015 doi: 10.1002-mrm.25711.
21. Tannus A, Garwood M. Improved performance of frequency-swept pulses using offset-independent adiabaticity. J Magn Reson Series A. 1996; 120:133–137.
22. Grant M, Boyd S. CVX: Matlab software for disciplined convex programming, version 2.0 beta. Sep.2013
23. Grant, M.; Boyd, S. Graph implementations for nonsmooth convex programs, Recent Advances in Learning and Control (a tribute to M. Vidyasagar). In: Blondel, V.; Boyd, S.; Kimura, H., editors. Lecture Notes in Control and Information Sciences. Springer; 2008. p. 95-110.
24. Rubner Y, Tomasi C, Guibas LJ. The earth mover's distance as a metric for image retrieval. Int Journal of Comp Vision. 2000; 40:99–121.

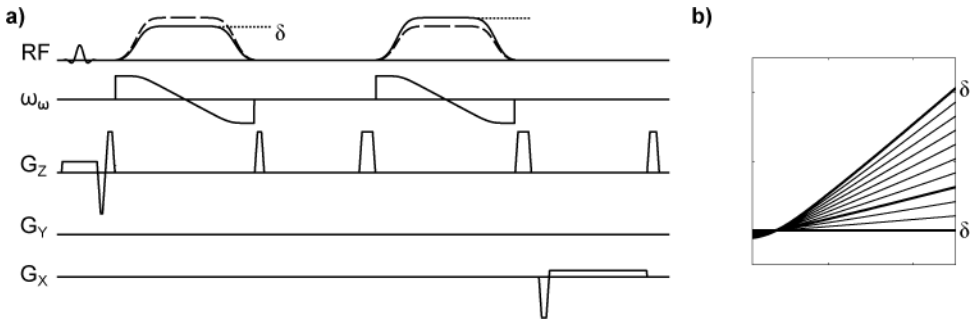

Fig. 1.

a. The BEAR sequence using HSn pulses is used to acquire B_1 projections with different values of δ, n_1 and n_2. A second projection is acquired for each set of parameters with the order of the adiabatic pulses reversed (dashed lines), and the phase difference between the two acquisitions is used to map to B_1, thereby removing any unwanted external phase sources that are present in both acquisitions. **b.** The phase sensitivity as a function of B_1 is plotted for different values of δ optimized for 3T, with δ=0.80,0.94,1 bolded.

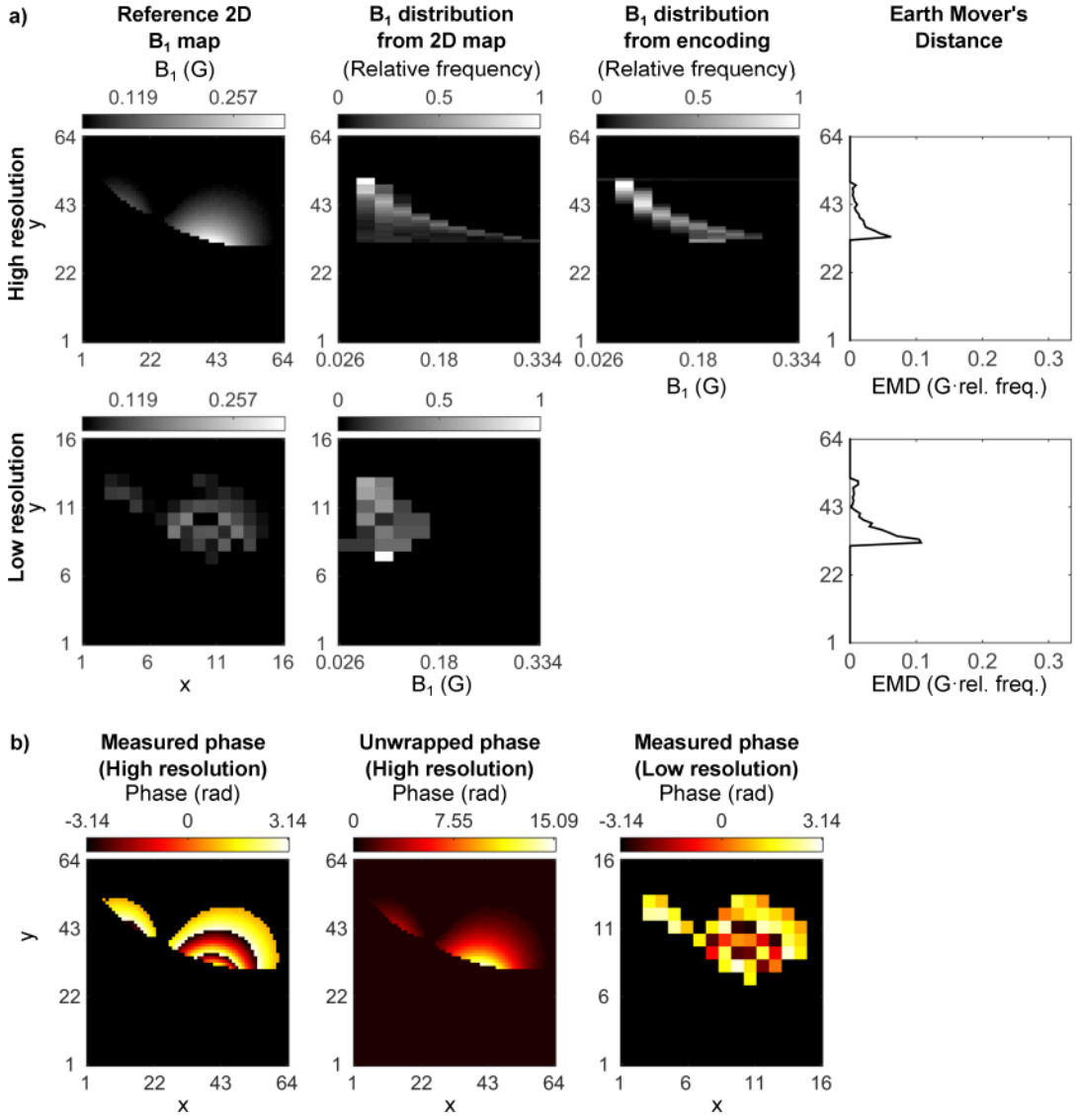

Fig. 2.

a. The relationship between a typical 2D B_1 map and a B_1 distribution plot is shown. Given the sequence in Figure 1a, let y represent the readout direction, which is resolved spatially for both image encoding and B_1 encoding. Each y location in the 2D B_1 map gives a 1D B_1 map, which can then be represented as a 1D B_1 distribution. The B_1 distribution plot displays the B_1 distribution for each y location as in the original 2D map. **b.** Acquisition and reconstruction strategy for the B_1 distribution plots. **i.** Shows an existing spatial B_1 variation in an object, and **ii.** shows three examples (δ=0.80,0.94,1) of the phase from the two acquired projections of Figure 1 (dashed gray and solid black lines). **iii.** Taking the inverse Fourier transform and phase difference converts each projection from k-space to image-space, which is used in Equation 4 to estimate **iv.**, the B_1 distribution in the imaging region.

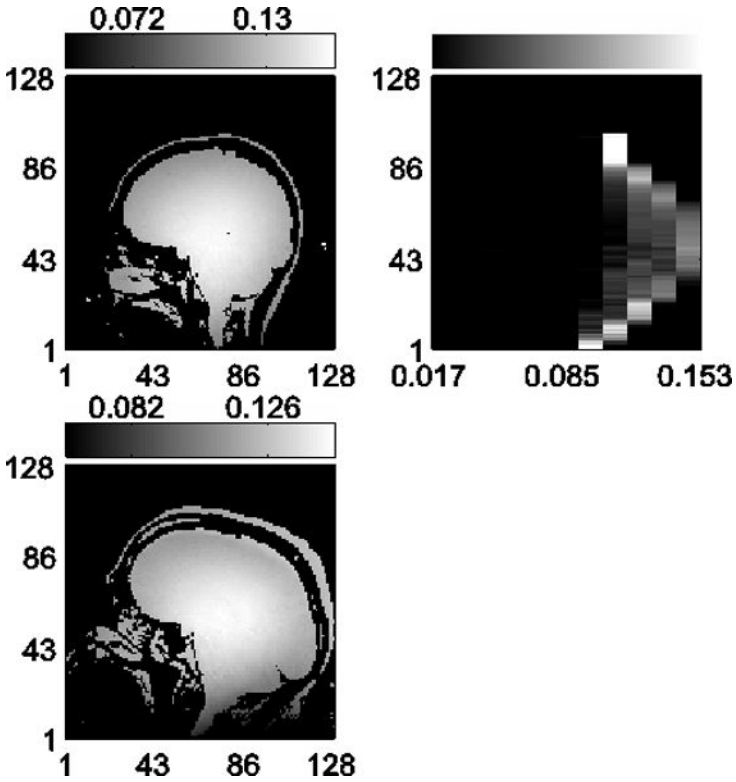

Fig. 3.

In vivo data results for B_1 distribution measurements at 3T. Shown are two representative datasets with (left to right): 2D B_1 maps acquired for reference, B_1 distributions calculated from the reference 2D maps, B_1 distributions using the encoding method proposed here, and EMD calculated between the two distributions. The mean EMD are 0.0022 G*(Relative frequency) and 0.0034 G*(Relative frequency) for top and bottom, respectively.

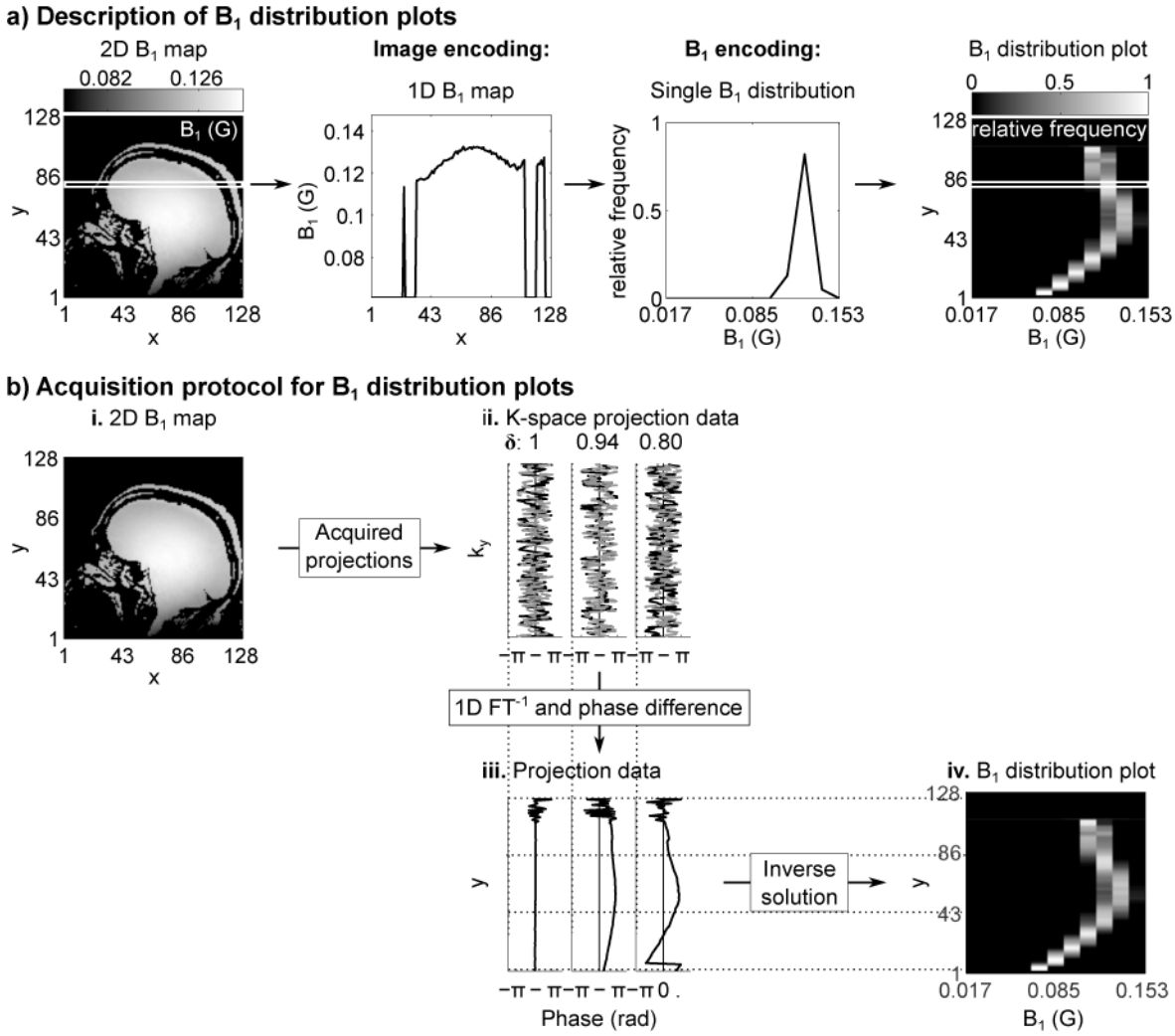

Fig. 4.

Phantom B_1 distribution results using a transmit and receive surface coil at 1.5T. Imaging used a wire along the surface of the phantom, placed perpendicular to the imaging plane and between the phantom and surface coil, to simulate increased B_1 variations in the presence of a guidewire. **a.** Shown are the 2D B_1 maps acquired at two different resolutions at an oblique slice to the surface coil to show large B_1 variation, as well as the B_1 distributions calculated from the 2D maps. The distribution using the encoding method proposed here is also shown, which uses fewer measurements than the lower resolution image, but has a mean EMD of 0.0136 G*(Relative frequency) whereas the average EMD for the low-resolution case, calculated by piecewise constant interpolation of the low-resolution image, is 0.0202 G*(Relative frequency).

b. Phase images of the acquired 2D maps are shown for both high- and low-resolution images. Due to the large B_1 range present in the imaging slice, phase wrapping occurs. This phase can be easily unwrapped for the high-resolution image, but not for the low-resolution image, causing increased errors in the B_1 approximation for the low-resolution image.

Table 1

HSn n_2 values for $n_1 = 4$ for varying δ and main-field strengths. The linear approximation of the sensitivity, α, is also given for each δ. For 1.5T, $B_{1,nom}$ = 0.086 G and the measured B_1 was expected to vary ±20%. For 3T, $B_{1;nom}$ = 0.12 G and the measured B_1 was expected to vary ±40%.

δ		0.80	0.82	0.84	0.86	0.88	0.90	0.92	0.94	0.96	0.98	1
1.5T	n_2	4.226	4.203	4.178	4.155	4.133	4.111	4.088	4.065	4.044	4.022	4
	α (rad/G)	90.4	81.6	72.6	63.7	54.7	45.7	36.6	27.5	18.4	9.20	0
3T	n_2	4.335	4.300	4.265	4.230	4.195	4.155	4.129	4.095	4.055	4.031	4
	α (rad/G)	98.6	88.9	79.1	69.2	59.4	49.3	39.7	29.7	19.6	9.92	0